ACS OMEGA

Open Access

http://pubs.acs.org/journal/acsodf

Article

Improved 3D−2D Perovskite for Efficient Perovskite Photovoltaics with Low-Temperature Carbon Electrodes

Jinxia Duan, Xiaoqing Li, Xiang Chen, Xiaoxin Pan, Xiaolu Xie, Yan Long, Yongcheng Wu, Houzhao Wan, Jun Zhang,* and Hao Wang*

Cite This: *ACS Omega* 2024, 9, 642−650

Read Online

ACCESS | Metrics & More | Article Recommendations | Supporting Information

ABSTRACT: Surface passivation and interface modification are effective strategies to acquire outstanding performances for perovskite solar cells (PeSCs). To suppress charge recombination and enhance the stability of the perovskite device, a hydrophobic two-dimensional (2D) perovskite is presented to construct a 3D−2D composite perovskite, passivating the perovskite surface/interfacial imperfection. Herein, a 3D−2D heterojunction perovskite is in situ synthesized on a 3D surface to maximize the charge transport and environmental stability. Through optimizing the annealing procedure systematically, the champion 3D−2D carbon-based PeSC achieves a power conversion efficiency of 17.95% and has wonderful long-term stability. Especially, an improved 3D−2D (3D−2D+) PeSC from restrict annealing even maintains 96.2% of the initial efficiency in air over 800 h and 90% efficiency under continuous 70 °C heating for 10 h owing to the passivation of the surface and thorough crystal boundary for the 3D−2D+ perovskite. The strong environmental stability of 3D−2D PeSCs has provided a wider avenue for fully low-temperature carbon-based PeSCs.

1. INTRODUCTION

The perovskite solar cells (PeSCs) have evolved miraculously into one star of state-of-the-art PeSCs for n−i−p configurated architectures. So far, the PeSCs have achieved exceptional power conversion efficiency (PCE) up to 26.08% (certified 25.73%), approaching single silicon and compound film photovoltaic cells.[1−3] The amazing progress propels the PeSCs toward the large-scalability and commercialization considering simple manufacture engineering and cheap ingredient costs.[3−6] Nevertheless, the device stability in the environment and structure matching needs to be further optimized for fulfilling the market request.[7,8] The classical high-efficiency PeSCs were fabricated with a spin-coated organic hole-transporting material (HTM) and evaporated metal electrode.[8−10] Metal electrodes from thermal evaporation or magnetic sputtering deteriorate PeSC performance owing to metal diffusion to HTM or perovskite.[2,10,11]

Commercial carbon paste is a challenging candidate as a PeSC electrode due to its stable structure, inexpensive cost, simple preparation, and low process temperatures. Low-temperature printable carbon electrodes have been employed to replace the metal electrode, which are extremely promising for commercialization and future wearables.[12−15] However, expensive organic HTM is susceptible and challenging, whose solvents are incompatible with low-temperature curable carbon pastes.[16] Carbon-based HTM-free PeSC (C-PeSC) was questioned considering interfacial recombination at the perovskite (PVK)/carbon interface. Chen et al. prepared improved C-PeSC by using an antisolvent dripping with the oxidized multiwalled carbon nanotubes (O-MWCNTs) attached. The cell efficiency reaches 8.99%. Unencapsulated devices maintain 80% of initial efficiency after 500 h at room temperature.[14] The device performance was visibly maximized due to prominent perovskite/carbon contact and quick charge transport between the perovskite and carbon electrode. Yu et al. reported that the $BMIMBF_4$ conditioner was employed to reduce PVK surface defects and mitigation the perovskite-carbon energy band mismatch. The corresponding $CsPbI_2Br$ C-PeSC obtained a high PCE of 14.03% and improved stability.[15]

Surface passivation of three-dimensional (3D) PVK absorbers is a feasible strategy to mitigate the nonradiate recombination at PVK/carbon interface and improve PVK quality. Hydrophobic two-dimensional (2D) perovskites were adopted to passivate the 3D perovskite surface because of their wider band gap and superior environmental stability.[17,18] 2D perovskites inhibit undesirable carrier recombination by reducing the surface/interface defect density, promoting hole extraction and electron blocking at the PVK/carbon interface.[19,20] For instance, Zhou et al. have reported that 2D-3D C-PeSCs with 2D $(EA)_2(MA)_{n-1}Pb_nI_{3n+1}$ (n = 6, 10, and 20) had a high efficiency above 11.88% and excellent environmental stability.[20] Zouhair et al. demonstrated that a 2D n-octylammonium iodide (OAI) layer was used as an electronic barrier layer to reduce the interface recombination loss. C-PeSC achieved the efficiency of 18.5% and a dramatically improved stability.[21] Chen et al. introduced a two-dimensional

Received: August 24, 2023
Revised: December 4, 2023
Accepted: December 12, 2023
Published: December 29, 2023

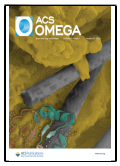

https://doi.org/10.1021/acsomega.3c06322
ACS Omega 2024, 9, 642−650

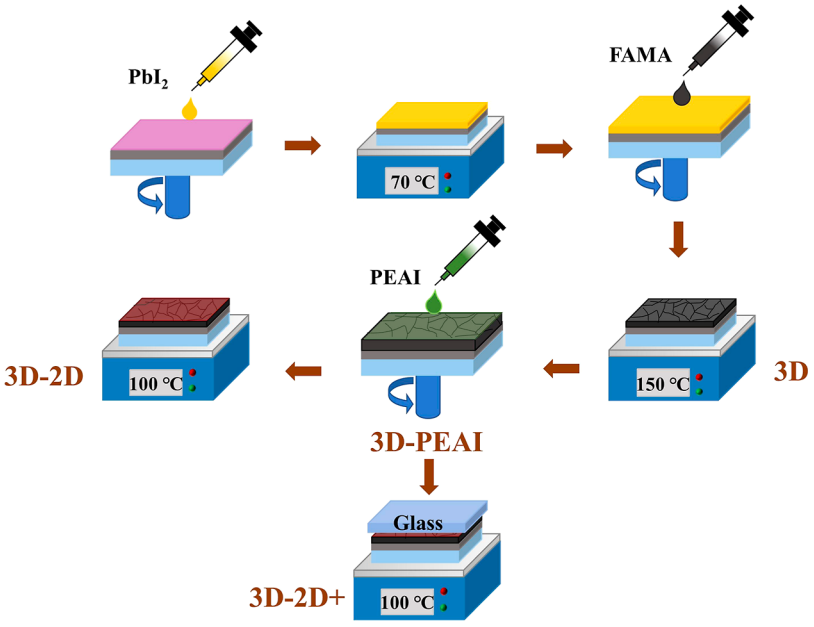

Figure 1. Schematic diagram of perovskite preparation.

(F5PEAI) layer to facilitate hole collection and prevent the electron from diffusing to the carbon end. Finally, the C-PeSCs reached a 16.24% efficiency.[22] Cao et al. developed a defect engineering to diminish 3D $MAPbI_3$ surface and crystal boundary deficiency and raise the quality and hydrophobicity of the PVK film, improving PCE and stability of the prepared C-PeSC.[23] 2D layered perovskite possesses greater freedom of chemical composition, stronger moisture resistance, and larger formation energy, which would effectively suppress perovskite surface contact with moisture and oxygen, interior ion migration generating the defects (vacancy defects, antisite defects, and so on), and nonradiate recombination.[24] Thus, the 2D perovskite materials deserve further development and research in C-PeSCs. The 3D−2D composite perovskite is an appropriate choice as an absorption layer to manufacture C-PeSCs, which would own an excellent carbon/perovskite interface and suppressed carrier recombination.[25]

Herein, the 2D perovskite was synthesized on-site on the surface of the 3D perovskite to transport holes and passivate 3D perovskite traps in low-temperature C-PeSCs. 2D perovskite was acquired by spin-coating 2-phenylethylamine hydroiodide (PEAI) above 3D formamidinium methylammonium lead iodide ($FAMAPbI_3$). Through altering annealing process systematically, different 3D−2D composite structures have been prepared. Ulteriorly, fully low-temperature C-PeSCs with 3D−2D perovskites and nanorods (NRs) electron transport layer (ETL) were fabricated. The mechanism of improved 3D−2D passivation and the photovoltaic properties of low-temperature C-PeSC were measured and explored.

2. EXPERIMENTAL SECTION

2.1. Materials. Titanium(IV) chloride ($TiCl_4$, CR), Tetrabutyl titanate ($C_{16}H_{36}O_4Ti$, 98%), and hydrochloric acid (HCl 36−38%) were obtained from Sinopharm Chemical Regent Co. Tin chloride ($SnCl_4$, 98%) was purchased from McLean. Methylammonium iodide (MAI, 99.8%), formamidinium iodide (FAI, 99.5%), methylammonium chloride (MACl, 99.9%), and lead iodide (PbI_2, 99.99%) were purchased from Xi'an Polymer Light Technology Corp. *N*,*N*-dimethylformamide (DMF, 99.9%), dimethyl sulfoxide (DMSO, 99.9%), and isopropanol (IPA, ≥99.7%) were purchased from Sigma-Aldrich. Phenylethylammonium iodide (PEAI, 98%) were obtained from Greatcell solar. Low temperature carbon paste was purchased from Shanghai MaterWin New Materials Co.

2.2. Device Fabrication. TiO_2 NAs were prepared on the basis of our previous report.[26] After the TiO_2 barrier layer (c-TiO_2) and NAs were grown, the $SnCl_4$ layer was deposited by the water bath method. 1 mL of $SnCl_4$ was dropped into 200 mL of deionized water and stirred until fully mixed. Then, TiO_2 NAs wafer was immersed in a sealed $SnCl_4$ solution and heated in a 70 °C water bath for 2 h. The eventual TiO_2/SnO_2 ETL had been obtained after annealing at 150 °C for 2 h.

The substrate was treated in ultraviolet ozone for 15 min prior to the deposition of PVK films. 3D PVK was synthesized by sequence spin-coating in air. Dissolve 692 mg of PbI_2 powder to 1 mL of solvent (V_{DMF}/V_{DMSO} = 9:1), stir evenly, and filter. 90 mg of FAI, 9 mg of MACl, and 6.39 mg of MAI were mixed in 1 mL of IPA to make organic salt solution. PbI_2 solution was spin-cast on the wafer at 1500 rpm for 35 s and heated at 72 °C for 12 s. The organic salt solution was then rotated on the PbI_2 product and heated at 152 °C for 30 min. Then, 10 mg/mL PEAI dissolved in IPA was cast at 4600 rpm for 30 s. Uniform and dense 2D/3D perovskite layers were formed by heating at 100 °C for 10 min. A carbon paste was printed on the PVK layer and heat-treated at 105 °C for 12 min. All experimental procedures were finished under the ambient air and 25−30% humidity. The active area of the devices is 0.06 cm^2.

2.3. Characterization. The plane-view and cross-sectional pictures were investigated by scanning electron microscopy (SEM) (JSM-7100F). The X-ray diffraction (XRD) patterns of PVK products were characterized by a D8 FOCUS X-ray diffractometer with Cu Kα radiation. Light absorption was determined by a UV−vis spectrophotometer (UV-3600, Shimadzu). The steady-state photoluminescence (PL) and time-resolved photoluminescence (TRPL) spectra of the PVK films were drawn using a steady state transient fluorescence spectrometer (Edinburgh FLS1000). The XPS spectra of the

https://doi.org/10.1021/acsomega.3c06322
ACS Omega 2024, 9, 642−650

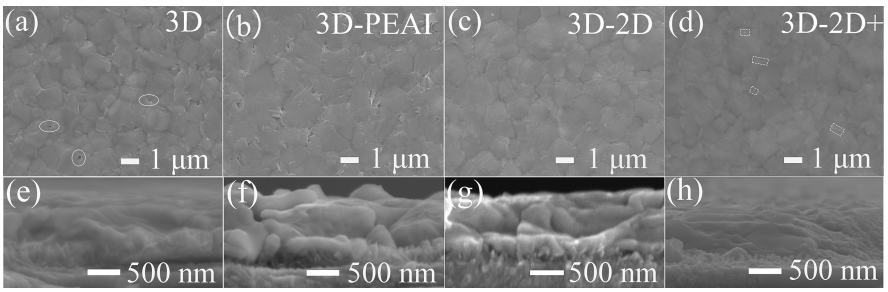

Figure 2. Top view SEM images of (a) 3D perovskite, (b) 3D-PEAI, (c) 3D−2D, and (d) 3D−2D+ perovskite films. Cross-sectional SEM images of (e) 3D perovskite, (f) 3D-PEAI, (g) 3D−2D, and (h) 3D−2D+ perovskite films.

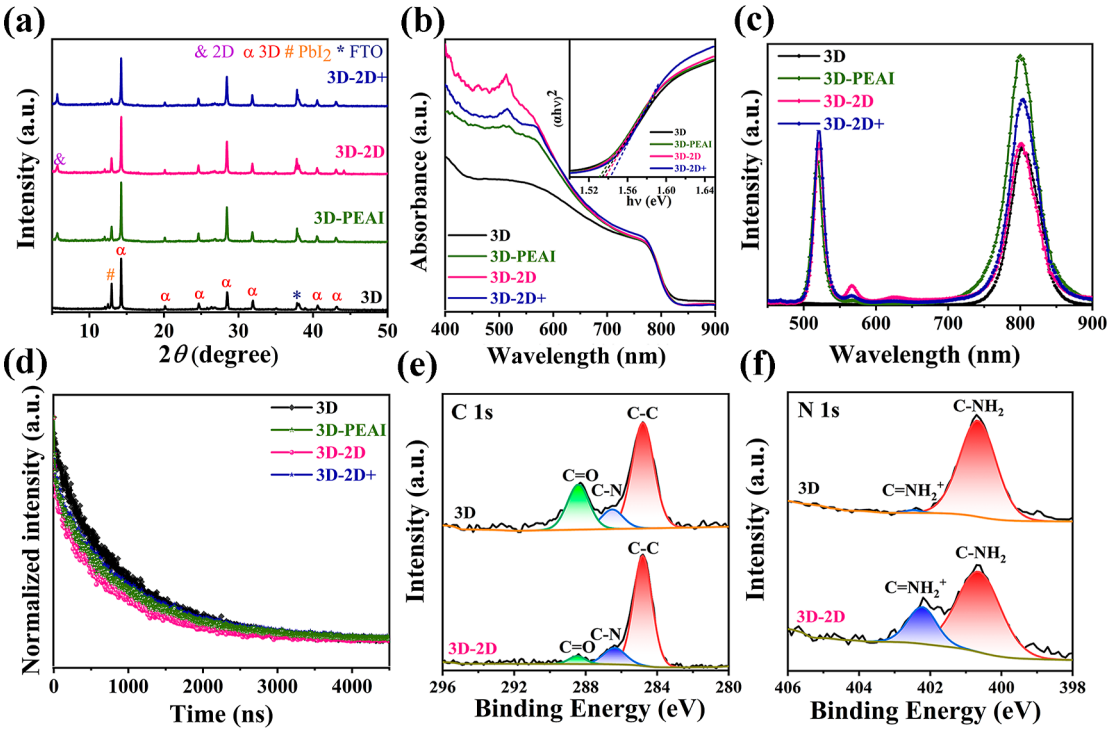

Figure 3. Optical characteristics of perovskite films: (a) XRD, (b) UV−vis, and Tauc plot, and (c) PL and (d) PL decay with the device structure of FTO/ETL/perovskite. XPS spectra of (e) C 1s and (f) N 1s.

samples were recorded using a XPS spectrometer (Thermo Fisher Scientific ESCALAB 250Xi). The photovoltaic properties and EQE were measured via a Keithley 2400 source meter and solar simulator (Newport 67005) under standard AM 1.5 G illumination. The PeSCs were scanned under reverse (1.4 V → −0.1 V, 50 mV/s) and forward direction (0.1 V → 1.4 V). The EIS plots and Schottky test of PeSCs were measured via an electrochemical workstation (CHI7601) in the dark. The water contact angle of PVK samples was measured by an OCA20 system.

3. RESULTS AND DISCUSSION

The surface imperfections of $FAMAPbI_3$ PVK films were passivated by an organic polymer molecule, such as phenylethylammonium iodide (PEAI). PEAI would react with residual PbI_2 to in situ form a 2D perovskite (PEA_2PbI_4) layer with/without heat annealing.[27] The corresponding products were obtained under different experimental conditions, shown in Figure 1 and Table S1.

To explore the effect of PEAI and heat temperature on the surficial topography of perovskite film, SEM tests were conducted on with and without post-treated perovskite samples. The surface topographies of PVK films with and without PEAI post-treatment are displayed in Figure 2. Uneven grain size and the existence of pores were detected in the surface of 3D PVK, as shown in Figure 2a. The grain size was 300−700 nm for the $FAMAPbI_3$ perovskite. Then, the surface topography of the 3D perovskite was almost completely covered with a macromolecule net structure for the 3D-PEAI sample. Through the annealing treatment, the compact and smooth film surface with the vivid grain boundary was obtained for the 3D−2D sample. The grain distribution of the 3D−2D perovskite was more uniform than that of the intrinsic $FAMAPbI_3$ film. The grain size of the 3D−2D product was 350−750 nm, slightly greater than $FAMAPbI_3$. Ulteriorly, the dense film was prepared for the 3D−2D+ sample by capping the upper surface with the glass sheet, accompanied by a whole lot of small particles. A considerable portion of grain boundaries in the 3D−2D+ film were blocked by small particles. To probe the effects of PEAI and heat-treatment on microstructure of PVK, cross-sectional images of perovskites

https://doi.org/10.1021/acsomega.3c06322
ACS Omega 2024, 9, 642−650

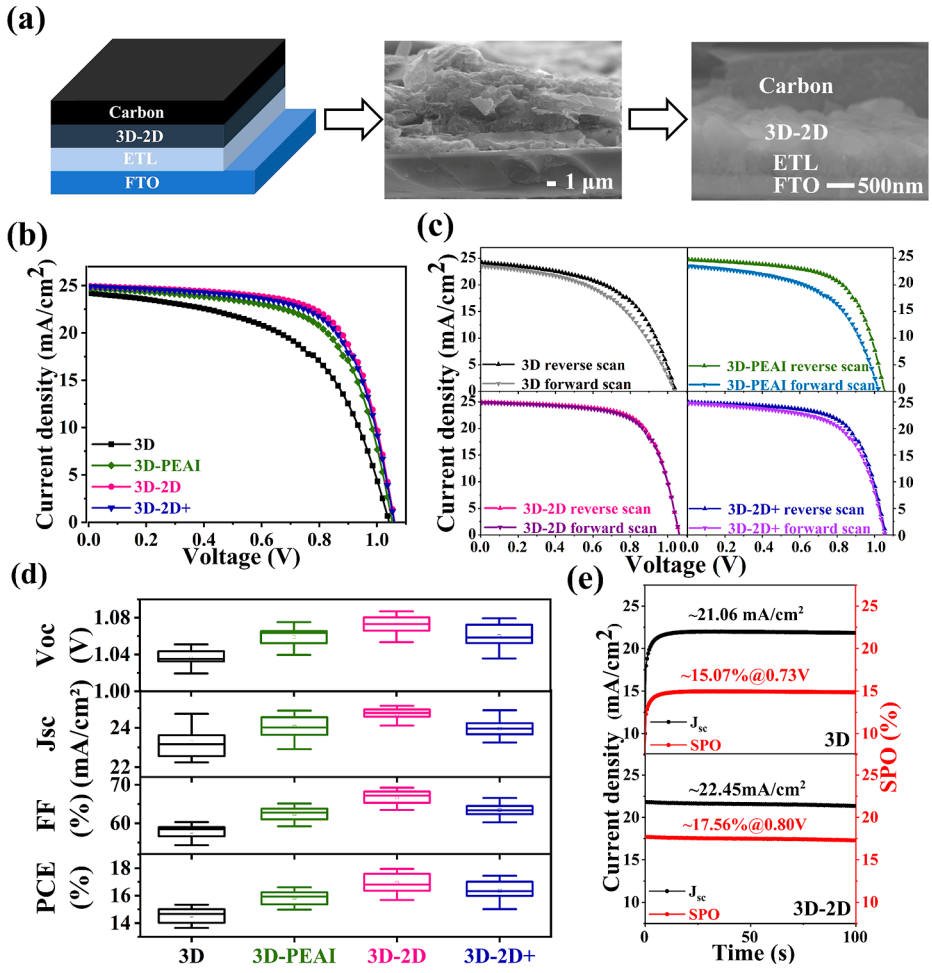

Figure 4. (a) Scheme and SEM images of the device structure. (b) $J-V$ curves of the devices. (c) RS and FS $J-V$ curves of the devices. (d) Box chart of V_{oc}, J_{sc}, FF, and PCE. (e) Steady-state power outputs at the maximum power point of 3D and 3D−2D.

are displayed in Figure 2e−h. The thickness of the four perovskite samples was ∼800 nm.

XRD patterns of four PVK specimens are shown in Figure 3a to explore the roles of PEAI post-treatment and heat-treatment on the PVK crystallization. The typical peaks of $FAMAPbI_3$ were inspected in the 3D perovskite film and identified by red α.[28] The accompanying peak at 12.7° indicated the PbI_2 residue in the PVK film. With PEAI addition, the intensity of α-$FAPbI_3$ peaks was raised, which was observed in 3D-PEAI, 3D−2D, and 3D−2D+ products. The intensity of the impurity PbI_2 peak decreased significantly in post-treated perovskite. The representative PEA_2PbI_4 (2D) peak at 5.53° existed in 3D-PEAI, 3D−2D, and 3D−2D+,[29] which proves that the 2D perovskite layer was formed on the 3D perovskite surface. The PbI_2 peak strength of the 3D−2D+ perovskite film was the weakest, indicating that the PbI_2 residual was the least. Subsequently, ultraviolet−visible (UV−vis) absorption curves for PVK samples are plotted in Figure 3b to measure the light capture ability. At 400−600 nm, the order of absorption intensity was 3D−2D > 3D−2D+ > 3D-PEAI > 3D. At 600−800 nm, the absorption intensity was 3D−2D+ > 3D−2D > 3D-PEAI > 3D. According to the curve of $(\alpha h\nu)^2-h\nu$ calculated based on the inset of Figure 3b, the corresponding energy bands of 3D, 3D-PEAI, 3D−2D, and 3D−2D+ were 1.534, 1.531, 1.536, and 1.542 eV, which was consistent with that of α-$FAMAPbI_3$ at 1.53 eV.[29] The typical 2D absorption peak at 513 nm (n = 1) and 566 nm (n = 2) were observed for the samples with the PEAI treatment.[31]

To fully analyze the charge transport and extraction of PVK films, PL and TRPL were performed on the samples. As shown in Figure 3c, post-treated perovskites had high 3D intrinsic emission peak, which meant that PEAI treatment could enhance the crystallinity of α-$FAPbI_3$. That was unanimous with the XRD consequences in Figure 3a. 3D-PEAI had the highest 3D intrinsic emission peak among the four films. The emission from the top 2D perovskite was clearly shown in PEAI-treated samples since PL spectra were recorded from the side of the perovskite. A remarkable emission peak at 520 nm, a weak one at 566 nm and a small shoulder at 627 nm were displayed, which corresponded to the emission for n = 1, 2, and 3 phases of quasi 2D perovskite, respectively.[30] 3D−2D+ had the strongest 2D (n = 1) emission among four films. TRPL was also fitted using a biexponential decay function in Figure 3d.[32] The fitting data are shown in Table S2. The corresponding computational lifetimes of 3D, 3D-PEAI, 3D−2D, and 3D−2D + were 955.96, 900.11, 810.91, and 938.49 ns, respectively. 3D−2D devices had the fastest decline rate, indicating that the photogenerated carrier transport was the quickest.

X-ray photoelectron spectroscopy (XPS) was further implemented on 3D and 3D−2D samples to prove the existence of 2D perovskite. The XPS results of the measured samples are shown in Figures S1 and 3. C−C (284.7 eV) and

https://doi.org/10.1021/acsomega.3c06322
ACS Omega 2024, 9, 642−650

Table 1. Photovoltaic Parameters of PeSCs

samples		V_{oc} (V)	J_{sc} (mA/cm^2)	FF (%)	PCE (%)	H
3D	FS Best	1.03	24.06	55.86	13.85	0.096
	RS Best	1.033	24.71	56.64	15.33	
	Ave.	1.035 ± 0.016	23.26 ± 1.45	57.86 ± 3.54	14.55 ± 0.90	
3D-PEAI	FS Best	1.02	24.17	61.21	14.88	0.104
	RS Best	1.052	24.72	63.81	16.61	
	Ave.	1.059 ± 0.02	24.05 ± 1.14	62.47 ± 3.27	15.88 ± 0.86	
3D−2D	FS Best	1.06	24.86	66.82	17.59	0.020
	RS Best	1.06	24.95	67.86	17.95	
	Ave.	1.072 ± 0.019	24.67 ± 0.7	66.74 ± 3.26	16.91 ± 1.23	
3D−2D+	FS Best	1.05	24.76	63.24	16.32	0.064
	RS Best	1.05	24.89	66.15	17.45	
	Ave.	1.059 ± 0.023	23.96 ± 0.93	63.48 ± 3.23	16.34 ± 1.33	

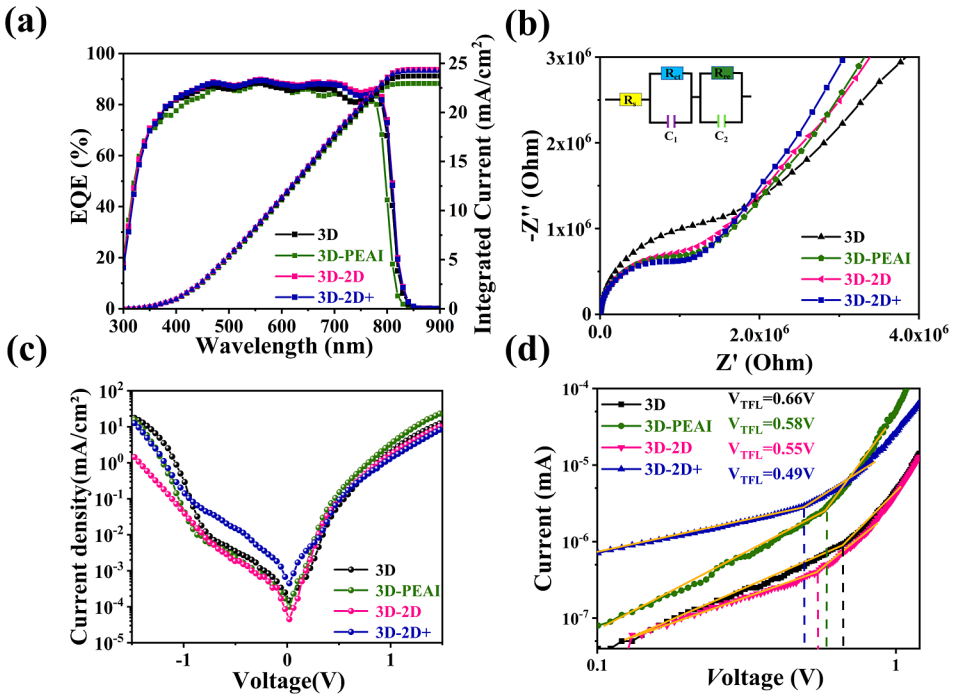

Figure 5. (a) EQE and integrated current density curves of the PeSCs. (b) Nyquist EIS spectra (the inset was the equivalent circuit), (c) dark $I-V$, and (d) SCLC curves of devices.

C−N (286.3 eV) bonds were detected in the C 1s spectrum for the 3D PVK film in Figure 3e, confirming the existence of FA^+/MA^+. As for C═O bond (288.4 eV) was regarded as the existence of the carbon oxide substances, which originated from 3D perovskite decomposition caused by the absorption of environmental moisture or oxygen.[33] The C−N (400.6 eV) and C═N (402.2 eV) characteristic bonds of FA^+ cations were found in the N 1s spectra of 3D PVK films (Figure 3f). In the N 1s spectrum of the 3D−2D film, the peak value of C═N increased significantly, which was consistent with the functional groups in PEA^+, confirming the formation of 3D−2D mixed PVK (Figure 3f). Notably, the C═O bond related to water-oxygen and decomposition in the original 3D perovskite was significantly reduced in the C 1s XPS of the 3D−2D PVK film, indicating a synergism of spatial impediment and sectional passivated the defects for 3D−2D PVK layers.[34]

HTM-free C-PeSCs were manufactured with an FTO/ETL/3D−2D/carbon sandwiched structure. The device structure diagram and SEM cross-sectional images of PeSC are presented in Figure 4a. The champion PeSC $J-V$ curves and related photovoltaic parameters were displayed in Figure 4b,c and Table 1. The champion PCEs of 3D, 3D-PEAI, 3D−2D, and 3D−2D+ were 15.33, 16.61, 17.95, and 17.45%, respectively, and the PEAI post-treatment enhanced the PeSC efficiency. 3D−2D and 3D−2D+ PeSCs had obviously improved PCE, which was attributed to defect reduction and recombination inhabitation by postannealing. For quantifying the hysteresis influence of PeSCs, the hysteresis factor (H) was estimated on the basis of reverse scanning (RS) and forward scanning (FS) data in Figure 4c.[35]

$$H = \frac{PCE_{RS} - PCE_{FS}}{PCE_{RS}} \quad (1)$$

where PCE_{RS} and PCE_{FS} are the efficiencies at RS and FS. The PCE_{RS} and PCE_{FS} of four PeSCs are listed in Figure 4b and Table 1. The hysteresis coefficients of PeSCs with 3D, 3D-PEAI, 3D−2D, and 3D−2D+ perovskite were 0.096, 0.104, 0.02, and 0.064, respectively. The short-circuit current density (J_{sc}), open-circuit voltage (V_{oc}), fill factor (FF), and PCE for 3D−2D PeSC were 24.86 mA/cm^2, 1.06 V, 66.82, and 17.59%

https://doi.org/10.1021/acsomega.3c06322
ACS Omega 2024, 9, 642−650

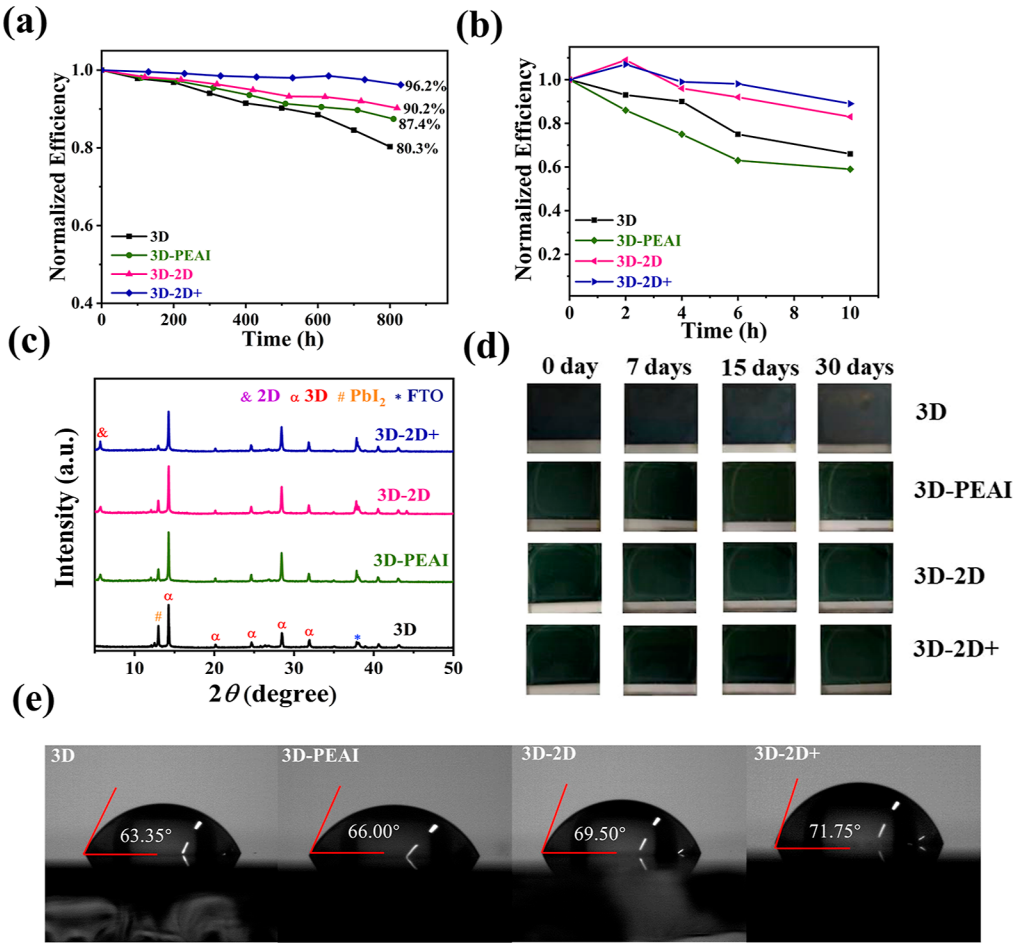

Figure 6. Stability tests of the devices: (a) stored at room temperature, (b) kept at 70 °C in air, the stability of the perovskite: (c) XRD spectra and (d) photos; (e) contact angle of perovskite films.

under FS scanning. 3D−2D cell harvested a V_{oc} of 1.06 V, a J_{sc} of 24.95 mA/cm^2, an FF of 67.86%, and a PCE of 17.95% at RS scanning. The 3D−2D device has the highest reverse PCE and lowest current hysteresis. The statistical photovoltaic coefficients are plotted in Figure 4d through synthesizing 15 equivalence PeSCs. PEAI-treated PeSCs had higher V_{oc}, J_{sc}, and FF values than untreated PeSCs. The PeSC with the 3D−2D perovskite had the highest FF, leading to the highest PCE. In addition, the stable photocurrent and power-output were implemented at a maximum power point voltage (V_{mp}) and 100 s illumination to test the light tolerance of the PeSCs. As shown in Figure 4e, the steady-state photocurrent and efficiency skyrocketed to the maximum. The stationary current densities were 21.06 and 22.45 mA/cm^2 for 3D and 3D−2D PeSCs. The eventual efficiencies for 3D and 3D−2D devices were 15.07 and 17.56%, which was in good agreement with the J−V results.

External quantum efficiency (EQE) and the integral J_{sc} for the PeSCs are depicted in Figure 5a. Integrated J_{sc} values of 3D, 3D-PEAI, 3D−2D, and 3D−2D+ based device were 23.71, 22.96, 24.39, and 24.23 mA/cm^2, similar to the actual measured J_{sc}. Electrochemical impedance spectra (EIS) for PeSCs are plotted in Figure 5b to investigate the charge transport of the samples with and without PEAI post-treatment. The recombination resistance (R_{re}) and transfer resistance (R_s) were estimated to investigate the internal and superficial carrier transportation. The fitting information is listed in Table S3. 3D−2D and 3D−2D+ based PeSCs had a smaller R_s and a larger R_{re} than the 3D cell, indicating that charge transport was modified both at the PVK interior and at the PVK/electrode interface for 3D−2D and 3D−2D+ based device.[28] That was the origin of strong FF, high efficiency, and slight hysteresis for 3D−2D and 3D−2D+ based PeSC. To investigate the operating mechanism of the PeSCs, the dark J−V plots are drawn in Figure 5c. The 3D−2D and 3D−2D+ PeSCs had relatively large saturation current (J_0) and shunt resistance (R_{sh}), which suggested that 3D−2D and 3D−2D+ PeSCs had high charge extraction and low current recombination as evidenced in Table S4. That was consistent with the results in absorption, PL, EIS, and J−V. The SCLC curve of the device was reflected in Figure 5d. Moreover, the trap density (N_{trap}) was counted by the space-charge limited current (SCLC)

$$N_{trap} = \frac{2\varepsilon_r\varepsilon_0 V_{TFL}}{eL^2} \quad (2)$$

where ε_r is PVK relative permittivity,[19] ε_0 is the vacuum permittivity, and L is the thickness for the PVK film (L = ∼800 nm). The trap-filled limit voltages (V_{TFL}) were 0.66, 0.58, 0.55, and 0.49 V, producing N_{trap} values of 3.65 × 10^{15}, 3.21 × 10^{15}, 3.04 × 10^{15}, and 2.71 × 10^{15} cm^{-3} for the reference 3D, 3D-PEAI, 3D−2D, and 3D−2D+ devices, respectively. 3D-based PeSC had the most the defect states, which were gradually eliminated during PEAI post-treatment. 3D−2D and 3D−2D+

https://doi.org/10.1021/acsomega.3c06322
ACS Omega 2024, 9, 642−650

Table 2. Recent Progress of 3D/2D Perovskite PeSCs with a Carbon Electrode

device structure	PCE	temperature (ETL, 3D/2D)	2D material	long-term stability	ref
FTO/mp-TiO_2/FAMA/2D/C	18.5%	high, low	OAI	82%, 500 h of sun illumination	21
FTO/TiO_2/FAMA/2D/C	15.6%		PEAI	80%, 40 ± 5% RH %, 700 h in ambient air	23
ITO/C_{60}/$(EA)_2(MA)PbI_3$/C	11.88%		EA	93%, 2160 h in ambient air 80% after heating at 80°C over 100 h 92%, 300 h of sun illuminatio	20
FTO/mp-TiO_2/$FAPbI_3$/3D/C	17.47%	high, low	F5PEAI	95%, 50−70 RH %, 100 h in ambient air 82%, in N_2 85%	22
FTO/TiO_2NRs/$FAPbI_3$/2D/C	17.95	Low, low	PEAI	90%, 30 ± 10% RH %, 800 h in air 85% after heating at 70°C over 10 h	this work
FTO/TiO_2NRs/$FAPbI_3$/2D+/C	17.45	Low, low	PEAI	96%, 30 ± 10% RH %, 800 h in air 90% after heating at 70°C over 10 h	this work

PeSCs had ratter less defect states, leading improved FF and suppressed hysteresis. In Mott−Schottky's curve of Figure S2, the larger horizontal coordinate corresponding to the intersection point of the tangent line and the horizontal line, the more difficult it is for the photogenerated carrier of the corresponding device to flow back from the electron transport layer to the PVK layer under sunlight irradiation, thus effectively improving V_{oc}.[36] In the light of Figure S2, The magnitude of the built-in potential was 3D−2D > 3D−2D+ > 3D-PEAI > 3D.

Based on the above results, the passivation function of PEAI and/or 2D was described presumptively in Figure S3. Shown in Figure S3 was healthy for PVK crystallization and carrier transportation, verified by improved XRD intensity ratio of α-phase/PbI_2 and 3D emission intensity for the 3D-PEAI sample. That was also the source of improved efficiency and stability for 3D-PEAI PeSC. For the 3D−2D sample, 2D passivation at the surface and partial boundaries remarkedly raise the PVK microstructure and charge transportation, proved by SEM, XRD, absorption, and PL tests. As a consequence, a high PCE of 17.95% and weak hysteresis were harvested. As for the 3D−2D+ sample, the surface and boundaries were completely passivated by 2D perovskite, resulting in high recombination resistance and low defect state density. Surface and boundary passivation was a powerful strategy to enhance the environmental stability of the PVK and PeSCs. Hydrophobic 2D perovskite passivation greatly improved moisture, oxygen, and thermal stability. Complete boundary passivation made the stability 3D−2D+ device superior to 3D−2D and the 3D-PEAI cell.

Thereafter, the long-term stability of perovskite devices was detected by storage in dark air conditions (RH = 20−30%), as shown in Figure 6a and Table 2. During monitoring, the efficiency of the 3D perovskite unit was rapidly lost, dropping to 80.3% of the initial efficiency after 800 h. PEAI treatment dramatically enhanced the PCE retention. 3D−2D PeSC displayed excellent stability and maintained ∼90.2% of the original value. 3D−2D+ device illustrated a quite outstanding stability, maintaining 96.2% initial efficiency after 800 h storage. The devices were also placed on a 70 °C hot table for 10 h to test their thermal stability in Figure 6b. 3D−2D+ PeSC surprisingly maintained 90% of initial efficiency, and the 3D−2D also retained 85% of initial PCE. However, the 3D device had only 65% PCE left. XRD test of environmental PVK tolerance was conducted, exhibited in Figure 6c. After storage for 7 days, an enhanced PbI_2 peak and reduced α-perovskite intensity were detected in the 3D perovskite, which suggested the degradation of the 3D perovskite film. The XRD patterns of 3D−2D and 3D−2D+ samples had no significant change during preservation for a period of time. Figure 6d displays the digital photos of the perovskite films placed at different times. After 15 days of placement, the black surface of the 3D perovskite gradually became light and began to degrade. After 30 days, the surrounding black phase degraded to reddish-brown, and the color of the central black phase became lighter. There were no significant changes in 3D−2D and 3D−2D+ perovskite films after 30 days of placement. The device performance after a certain number of days of storage is shown in Table S5. In addition, the hydrophobicity of the untreated and PEAI-treated samples was demonstrated by measuring the contact angle of water droplets on the film surface (Figure 6e). The contact angle for 3D PVK was 63.35°, while it increased to 71.75° for the 3D−2D+ film. The results showed that the hydrophobicity of the PEAI-treated samples was improved effectively. Ultimately, 3D−2D and 3D−2D+ films exhibited a rather positive moisture-stability than 3D films due to the hydrophobicity of 2D materials, which resulted in high environmental stability.[17]

Various PEAI concentrations were employed to prepare 3D−2D PVK and PeSCs to determine the optimal concentration. The PVK related to 5, 10, and 20 mg/mL PEAI were marked as 3D−2D (5), 3D−2D (10), and 3D−2D (20). The SEM images of 3D−2D PVK films with different PEAI contents are shown in Figure S4. The surface pinholes reduced, and the grain size distribution was uniform in 3D−2D (10). The cracks and poor film quality were displayed on the 3D−2D (20) surface due to PEAI agglomeration. In UV−vis spectra, 3D−2D (10) film had the strongest absorption ability in Figure S5a. 2D characteristic peak started to generate in 3D−2D (10), reflected by XRD patterns of Figure S5b. The PeSCs with various 3D−2D were manufactured, and then, the efficiency was measured in Figure S6 and Table S6. The maximum PCE were obtained for 3D−2D (10) PeSC. The PCE of 3D−2D (20) PeSC was the lowest among four samples, which was owing to thicker 2D perovskite or PEAI agglomeration hindering the carrier transport.

4. CONCLUSIONS

The 2D perovskite passivation layer was in situ synthesized on the 3D perovskite top surface to form a 3D/2D heterostructure. 3D-PEAI, 3D−2D, and 3D−2D+ heterostructures were obtained through adding PEAI without annealing, annealing, and restricted annealing, respectively. The 2D perovskite layer reduced the surface defect state density, improved carrier migration rate, accelerated internal charge transport, and inhibited nonradiative composite loss, thus

https://doi.org/10.1021/acsomega.3c06322
ACS Omega 2024, 9, 642−650

enhancing photovoltaic performances and stability. The champion 3D−2D device achieved a high PCE of 17.95% and weak lag. The equipment maintained an initial efficiency of about 90% at room temperature, darkness, and 20−30% relative humidity in the air environment for 800 h, showing good stability. In addition, improved 3D−2D+ cell with PCE of 17.45% maintained an initial efficiency of about 96.2% at room temperature, darkness, and 20−30% relative humidity in the air environment for 800 h. The efficiency of 90% was maintained after continuous heating at 70 °C for 10 h in air. The prominent stability of the 3D−2D+ device is due to complete boundary passivation of 3D−2D+ perovskite.

■ ASSOCIATED CONTENT

Supporting Information

The Supporting Information is available free of charge at https://pubs.acs.org/doi/10.1021/acsomega.3c06322.

Experimental parameters of perovskites; PL decay parameters of the samples; Nyquist EIS plot fitting results of the samples; dark $J-V$ curves fitting results of the samples; photovoltaic parameters of PeSCs stored at room temperature; photovoltaic parameters of PeSCs with different PEAI concentrations; XPS spectra of 3D and 3D−2D; Mott−Schottky's curves of the samples; schematic diagrams of 2D passivation on PeSCs; SEM images of PVK films with different PEAI concentrations; 3D−2D PVK films: absorption spectra and XRD patterns; and PCE of the PeSCs with 3D−2D perovskite (PDF)

■ AUTHOR INFORMATION

Corresponding Authors

Hao Wang − *Hubei Yangtze Memory Laboratories, Wuhan 430205, PR China; Institute of Microelectronics and Integrated Circuits, School of Microelectronics, Hubei University, Wuhan 430062, PR China;* orcid.org/0000-0001-8984-1508; Email: nanoguy@126.com

Jun Zhang − *Hubei Yangtze Memory Laboratories, Wuhan 430205, PR China; Institute of Microelectronics and Integrated Circuits, School of Microelectronics, Hubei University, Wuhan 430062, PR China;* Email: gwen_zhang@126.com

Authors

Jinxia Duan − *Hubei Yangtze Memory Laboratories, Wuhan 430205, PR China; Institute of Microelectronics and Integrated Circuits, School of Microelectronics, Hubei University, Wuhan 430062, PR China*

Xiaoqing Li − *Institute of Microelectronics and Integrated Circuits, School of Microelectronics, Hubei University, Wuhan 430062, PR China*

Xiang Chen − *Institute of Microelectronics and Integrated Circuits, School of Microelectronics, Hubei University, Wuhan 430062, PR China*

Xiaoxin Pan − *Institute of Microelectronics and Integrated Circuits, School of Microelectronics, Hubei University, Wuhan 430062, PR China*

Xiaolu Xie − *Institute of Microelectronics and Integrated Circuits, School of Microelectronics, Hubei University, Wuhan 430062, PR China*

Yan Long − *Institute of Microelectronics and Integrated Circuits, School of Microelectronics, Hubei University, Wuhan 430062, PR China*

Yongcheng Wu − *Institute of Microelectronics and Integrated Circuits, School of Microelectronics, Hubei University, Wuhan 430062, PR China*

Houzhao Wan − *Hubei Yangtze Memory Laboratories, Wuhan 430205, PR China; Institute of Microelectronics and Integrated Circuits, School of Microelectronics, Hubei University, Wuhan 430062, PR China;* orcid.org/0000-0001-7586-7723

Complete contact information is available at: https://pubs.acs.org/10.1021/acsomega.3c06322

Author Contributions

The manuscript was written through contributions of all authors. All authors have given approval to the final version of the manuscript.

Notes

The authors declare no competing financial interest.

■ ACKNOWLEDGMENTS

This work was aided financially by the National Natural Science Foundation of China (no. 11874143), Hubei Provincial Department of Educational of China (no. D20191005), and Application Fundamental Research Project of Wuhan Science and Technology Bureau (no. 2019010701011396).

■ REFERENCES

(1) Jeong, J.; Kim, M.; Seo, J.; Lu, H.; Ahlawat, P.; Mishra, A.; Yang, Y.; Hope, M. A.; Eickemeyer, F. T.; Kim, M.; Yoon, Y. J.; Choi, I. W.; Darwich, B. P.; Choi, S. J.; Jo, Y.; Lee, J. H.; Walker, B.; Zakeeruddin, S. M.; Emsley, L.; Rothlisberger, U.; Hagfeldt, A.; Kim, D. S.; Grätzel, M.; Kim, J. Y. Pseudo-Halide Anion Engineering for α-$FAPbI_3$ Perovskite Solar Cells. *Nature* **2021**, *592*, 381−385.

(2) Kim, M.; Jeong, J.; Lu, H.; Lee, T. K.; Eickemeyer, F. T.; Liu, Y.; Choi, I. W.; Choi, S. J.; Jo, Y.; Kim, H.-B.; Mo, S.-I.; Kim, Y.-K.; Lee, H.; An, N. G.; Cho, S.; Tress, W. R.; Zakeeruddin, S. M.; Hagfeldt, A.; Kim, J. Y.; Grätzel, M.; Kim, D. S. Conformal Quantum Dot-SnO_2 Layers as Electron Transporters for Efficient Perovskite Solar Cells. *Science* **2022**, *375* (6578), 302−306.

(3) Park, J.; Kim, J.; Yun, H.-S.; Paik, M. J.; Noh, E.; Mun, H. J.; Kim, M. G.; Shin, T. J.; Seok, S. I. Controlled Growth of Perovskite Layers with Volatile Alkylammonium Chlorides. *Nature* **2023**, *616* (7958), 724−730.

(4) Azmi, R.; Ugur, E.; Seitkhan, A.; Aljamaan, F.; Subbiah, A. S.; Liu, J.; Harrison, G. T.; Nugraha, M. I.; Eswaran, M. K.; Babics, M.; Chen, Y.; Xu, F.; Allen, T. G.; Rehman, A. U.; Wang, C.-L.; Anthopoulos, T. D.; Schwingenschlögl, U.; De Bastiani, M.; Aydin, E.; De Wolf, S. Damp Heat-Stable Perovskite Solar Cells with Tailored-Dimensionality 2D/3D Heterojunctions. *Science* **2022**, *376* (6588), 73−77.

(5) Sachith, B. M.; Okamoto, T.; Ghimire, S.; Umeyama, T.; Takano, Y.; Imahori, H.; Biju, V. Long-Range Interfacial Charge Carrier Trapping in Halide Perovskite-C_{60} and Halide Perovskite-TiO_2 Donor-Acceptor Films. *J. Phys. Chem. Lett.* **2021**, *12* (35), 8644−8651.

(6) Shahjahan, M. D.; Okamoto, T.; Chouhan, L.; Sachith, B. M.; Pradhan, N.; Misawa, H.; Biju, V. Halide Perovskite Single Crystals and Nanocrystal Films as Electron Donor-Acceptor Heterojunctions. *Angew. Chem., Int. Ed.* **2023**, *62* (4), No. e202215947.

(7) Chouhan, L.; Ghimire, S.; Subrahmanyam, C.; Miyasaka, T.; Biju, V. Synthesis, Optoelectronic Properties and Applications of Halide Perovskites. *Chem. Soc. Rev.* **2020**, *49* (10), 2869−2885.

(8) Duong, T.; Nguyen, T.; Huang, K.; Pham, H.; Adhikari, S. G.; Khan, M. R.; Duan, L.; Liang, W.; Fong, K. C.; Shen, H.; Bui, A. D.; Mayon, A. O.; Truong, T.; Tabi, G.; Ahmad, V.; Surve, S.; Tong, J.; Kho, T.; Tran-Phu, T.; Lu, T.; Zheng, J.; Paetzold, U. W.; Lemmer, U.; Baillie, A. H.; Liu, Y.; Andersson, G.; White, T.; Weber, K.; Catchpole, K. Bulk Incorporation with 4-Methylphenethylammonium Chloride for Efficient and Stable Methylammonium-Free Perovskite and Perovskite-Silicon Tandem Solar Cells. *Adv. Energy Mater.* **2023**, *13* (9), 2203607.
(9) Wu, T.; Ono, L. K.; Yoshioka, R.; Ding, C.; Zhang, C.; Mariotti, S.; Zhang, J.; Mitrofanov, K.; Liu, X.; Segawa, H.; Kabe, R.; Han, L.; Qi, Y. Elimination of Light-Induced Degradation at the Nickel Oxide-Perovskite Heterojunction by Aprotic Sulfonium Layers towards Long-Term Operationally Stable Inverted Perovskite Solar Cells. *Energy Environ. Sci.* **2022**, *15* (11), 4612−4624.
(10) Wang, X.; Wang, L.; Shan, T.; Leng, S.; Zhong, H.; Bao, Q.; Lu, Z.-H.; Deng, L.-L.; Chen, C.-C. Low-Temperature Aging Provides 22% Efficient Bromine-Free and Passivation Layer-Free Planar Perovskite Solar Cells. *Nano-Micro Lett.* **2020**, *12* (1), 84.
(11) Min, H.; Lee, D. Y.; Kim, J.; Kim, G.; Lee, K. S.; Kim, J.; Paik, M. J.; Kim, Y. K.; Kim, K. S.; Kim, M. G.; Shin, T. J.; Il Seok, S. Perovskite Solar Cells with Atomically Coherent Interlayers on SnO_2 Electrodes. *Nature* **2021**, *598* (7881), 444−450.
(12) Bogachuk, D.; Zouhair, S.; Wojciechowski, K.; Yang, B.; Babu, V.; Wagner, L.; Xu, B.; Lim, J.; Mastroianni, S.; Pettersson, H.; et al. Low-temperature carbon-based electrodes in perovskite solar cells. *Energy Environ. Sci.* **2020**, *13* (11), 3880−3916.
(13) Omrani, M.; Keshavarzi, R.; Abdi-Jalebi, M.; Gao, P. Impacts of Plasmonic Nanoparticles Incorporation and Interface Energy Alignment for Highly Efficient Carbon-Based Perovskite Solar Cells. *Sci. Rep.* **2022**, *12* (1), 5367.
(14) Chen, R.; Feng, Y.; Zhang, C.; Wang, M.; Jing, L.; Ma, C.; Bian, J.; Shi, Y. Carbon-Based HTL-Free Modular Perovskite Solar Cells with Improved Contact at Perovskite/Carbon Interfaces. *J. Mater. Chem. C* **2020**, *8* (27), 9262−9270.
(15) Yu, F.; Han, Q.; Wang, L.; Yang, S.; Cai, X.; Zhang, C.; Ma, T. Surface Management for Carbon-Based $CsPbI_2Br$ Perovskite Solar Cell with 14% Power Conversion Efficiency. *Sol. RRL* **2021**, *5* (9), 2100404.
(16) Wang, Y.; Li, W.; Yin, Y.; Wang, M.; Cai, W.; Shi, Y.; Guo, J.; Shang, W.; Zhang, C.; Dong, Q.; Ma, H.; Liu, J.; Tian, W.; Jin, S.; Bian, J.; Shi, Y. Defective MWCNT Enabled Dual Interface Coupling for Carbon-Based Perovskite Solar Cells with Efficiency Exceeding 22%. *Adv. Funct. Mater.* **2022**, *32* (31), 2204831.
(17) Paek, S.; Roldán-Carmona, C.; Cho, K. T.; Franckevičius, M.; Kim, H.; Kanda, H.; Drigo, N.; Lin, K.; Pei, M.; Gegevičius, R.; Yun, H. J.; Yang, H.; Schouwink, P. A.; Corminboeuf, C.; Asiri, A. M.; Nazeeruddin, M. K. Molecular Design and Operational Stability: Toward Stable 3D/2D Perovskite Interlayers. *Adv. Sci.* **2020**, *7* (19), 2001014.
(18) McGott, D. L.; Muzzillo, C. P.; Perkins, C. L.; Berry, J. J.; Zhu, K.; Duenow, J. N.; Colegrove, E.; Wolden, C. A.; Reese, M. O. 3D/2D Passivation as a Secret to Success for Polycrystalline Thin-Film Solar Cells. *Joule* **2021**, *5* (5), 1057−1073.
(19) Li, J.; Wu, M.; Yang, G.; Zhang, D.; Wang, Z.; Zheng, D.; Yu, J. Bottom-up Passivation Effects by Using 3D/2D Mix Structure for High Performance p-i-n Perovskite Solar Cells. *Sol. Energy* **2020**, *205*, 44−50.
(20) Zhou, J.; Ye, Z.; Hou, J.; Wu, J.; Zheng, Y.-Z.; Tao, X. Efficient Ambient-Air-Stable HTM-Free Carbon-Based Perovskite Solar Cells with Hybrid 2D-3D Lead Halide Photoabsorbers. *J. Mater. Chem. A* **2018**, *6* (45), 22626−22635.
(21) Zouhair, S.; Yoo, S.; Bogachuk, D.; Herterich, J. P.; Lim, J.; Kanda, H.; Son, B.; Yun, H. J.; Würfel, U.; Chahboun, A.; Nazeeruddin, M. K.; Hinsch, A.; Wagner, L.; Kim, H. Employing 2D-Perovskite as an Electron Blocking Layer in Highly Efficient (18.5%) Perovskite Solar Cells with Printable Low Temperature Carbon Electrode. *Adv. Energy Mater.* **2022**, *12* (21), 2200837.
(22) Chen, X.; Xia, Y.; Huang, Q.; Li, Z.; Mei, A.; Hu, Y.; Wang, T.; Cheacharoen, R.; Rong, Y.; Han, H. Tailoring the Dimensionality of Hybrid Perovskites in Mesoporous Carbon Electrodes for Type-II Band Alignment and Enhanced Performance of Printable Hole-Conductor-Free Perovskite Solar Cells. *Adv. Energy Mater.* **2021**, *11* (18), 2100292.
(23) Cao, D.; Li, Z.; Xu, Y.; Li, W.; Zhong, H.; Huang, Y.; Zhang, X.; Wan, L.; Zhang, X.; Li, Y.; Ren, X.; Wang, X.; Eder, D.; Wang, S. Interfacial Engineering by P-Methylphenylmethylammonium Iodide for Efficient Carbon Counter Electrode (CE)-Based 2D/3D Hybrid Perovskite Solar Cells. *Org. Electron.* **2023**, *113*, 106699.
(24) Ye, T.; Hou, Y.; Nozariasbmarz, A.; Yang, D.; Yoon, J.; Zheng, L.; Wang, K.; Wang, K.; Ramakrishna, S.; Priya, S. Cost-Effective High-Performance Charge-Carrier-Transport-Layer-Free Perovskite Solar Cells Achieved by Suppressing Ion Migration. *ACS Energy Lett.* **2021**, *6* (9), 3044−3052.
(25) Wang, Z.; Lin, Q.; Chmiel, F. P.; Sakai, N.; Herz, L. M.; Snaith, H. J. Efficient Ambient-Air-Stable Solar Cells with 2D-3D Heterostructured Butylammonium-Caesium-Formamidinium Lead Halide Perovskites. *Nat. Energy* **2017**, *2* (9), 17135.
(26) Duan, J.; Xie, X.; Yang, Y.; Wan, H.; Ma, G.; Shen, L.; Zhang, J.; Tao, L.; Wang, H.; Zhou, H. High-Efficiency α-$FAPbI_3$ Perovskite Solar Cells Based on One-Dimensional TiO2 Nanorod Array Scaffolds. *Org. Electron.* **2023**, *114*, 106750.
(27) Lee, M.; Choi, E.; Soufiani, A. M.; Lim, J.; Kim, M.; Chen, D.; Green, M. A.; Seidel, J.; Lim, S.; Kim, J.; Dai, X.; Lee-Chin, R.; Zheng, B.; Hameiri, Z.; Park, J.; Hao, X.; Yun, J. S. Enhanced Hole-Carrier Selectivity in Wide Bandgap Halide Perovskite Photovoltaic Devices for Indoor Internet of Things Applications. *Adv. Funct. Mater.* **2021**, *31* (16), 2008908.
(28) Zhan, S.; Duan, Y.; Liu, Z.; Yang, L.; He, K.; Che, Y.; Zhao, W.; Han, Y.; Yang, S.; Zhao, G.; Yuan, N.; Ding, J.; Liu, S. (F.). Stable 24.29%-Efficiency $FA_{0.85}MA_{0.15}PbI_3$ Perovskite Solar Cells Enabled by Methyl Haloacetate-Lead Dimer Complex. *Adv. Energy Mater.* **2022**, *12* (27), 2200867.
(29) Sutanto, A. A.; Szostak, R.; Drigo, N.; Queloz, V. I. E.; Marchezi, P. E.; Germino, J. C.; Tolentino, H. C. N.; Nazeeruddin, M. K.; Nogueira, A. F.; Grancini, G. In Situ Analysis Reveals the Role of 2D Perovskite in Preventing Thermal-Induced Degradation in 2D/3D Perovskite Interfaces. *Nano Lett.* **2020**, *20* (5), 3992−3998.
(30) Niu, T.; Lu, J.; Jia, X.; Xu, Z.; Tang, M.-C.; Barrit, D.; Yuan, N.; Ding, J.; Zhang, X.; Fan, Y.; Luo, T.; Zhang, Y.; Smilgies, D.-M.; Liu, Z.; Amassian, A.; Jin, S.; Zhao, K.; Liu, S. Interfacial Engineering at the 2D/3D Heterojunction for High-Performance Perovskite Solar Cells. *Nano Lett.* **2019**, *19* (10), 7181−7190.
(31) Jiang, Q.; Zhao, Y.; Zhang, X.; Yang, X.; Chen, Y.; Chu, Z.; Ye, Q.; Li, X.; Yin, Z.; You, J. Surface Passivation of Perovskite Film for Efficient Solar Cells. *Nat. Photonics* **2019**, *13* (7), 460−466.
(32) Mohammed, M. K. A.; Esmail Shalan, A.; Dehghanipour, M.; Mohseni, H. R. Improved Mixed-Dimensional 3D/2D Perovskite Layer with Formamidinium Bromide Salt for Highly Efficient and Stable Perovskite Solar Cells. *Chem. Eng. J.* **2022**, *428*, 131185.
(33) Chen, P.; Bai, Y.; Wang, S.; Lyu, M.; Yun, J.; Wang, L. In Situ Growth of 2D Perovskite Capping Layer for Stable and Efficient Perovskite Solar Cells. *Adv. Funct. Mater.* **2018**, *28* (17), 1706923.
(34) Aristidou, N.; Eames, C.; Sanchez-Molina, I.; Bu, X.; Kosco, J.; Islam, M. S.; Haque, S. A. Fast Oxygen Diffusion and Iodide Defects Mediate Oxygen-Induced Degradation of Perovskite Solar Cells. *Nat. Commun.* **2017**, *8* (1), 15218.
(35) Liu, P.; Wang, W.; Liu, S.; Yang, H.; Shao, Z. Fundamental Understanding of Photocurrent Hysteresis in Perovskite Solar Cells. *Adv. Energy Mater.* **2019**, *9* (13), 1803017.
(36) Prochowicz, D.; Tavakoli, M. M.; Solanki, A.; Goh, T. W.; Pandey, K.; Sum, T. C.; Saliba, M.; Yadav, P. Understanding the effect of chlorobenzene and isopropanol anti-solvent treatments on the recombination and interfacial charge accumulation in efficient planar perovskite solar cells. *J. Mater. Chem. A* **2018**, *6* (29), 14307−14314.

https://doi.org/10.1021/acsomega.3c06322
ACS Omega 2024, 9, 642−650